Composites Science and Technology 232 (2023) 109850

Contents lists available at ScienceDirect

Composites Science and Technology

journal homepage: www.elsevier.com/locate/compscitech

Electrically conductive and 3D-printable copolymer/MWCNT nanocomposites for strain sensing

Iee Lee Hia [a], Alexander D. Snyder [b], Jack S. Turicek [b], Fernanda Blanc [a], Jason F. Patrick [c,*], Daniel Therriault [a,*]

[a] Laboratory for Multiscale Mechanics, Centre for High Performance Polymer and Composite Systems (CREPEC), Department of Mechanical Engineering, Montreal, H3T 1J4, Quebec, Canada
[b] Department of Mechanical and Aerospace Engineering, North Carolina State University, Raleigh, 27695, North Carolina, USA
[c] Department of Civil, Construction, and Environmental Engineering, North Carolina State University, Raleigh, 27695, North Carolina, USA

ARTICLE INFO

Keywords:
Additive manufacturing
Multi-walled carbon nanotubes
Piezoresistivity
Fiber-reinforced polymer composite
Structural health monitoring

ABSTRACT

Structural health monitoring (SHM) of safety-critical composite components is essential to ensure mechanical stasis and detect local damage before it can produce global failure. SHM technologies must also adapt to ever-evolving materials and geometries, but traditional piezoresistive strain sensors lack the ability for end-user customization and modifications throughout service-life. Additive manufacturing via fused filament fabrication (FFF) provides a practical pathway to overcome such sensor shortcomings. However, the electrical conductivity of conventional polymer feedstock is not sufficient for accurate strain measurements without compromise to melt viscosity and thus printability. Here we report the development of a new 3D-printable and electrically responsive nanocomposite by melt-mixing poly(ethylene-co-methacrylic acid) (EMAA) with multi-walled carbon nanotubes (MWCNT). Bulk electrical conductivity of 43.9 S m^{-1} is achieved at only 5 wt% loading – higher than comparable materials – where the nano-dispersion heterogeneity of MWCNT in EMAA is linked to the favorable conductivity while retaining molten flowability. FFF is employed to print thin (150 μm) serpentine strain sensors onto the surface of a glass fiber-reinforced polymer composite, which exhibit strong adhesion and accurate piezoresistive sensing under cyclic flexural loading. Twenty consecutive cycles with converged sensor readings (i.e., < 1% variation in measured resistance) demonstrates reliable performance across a relevant service strain range (0.4 – 0.8 %) for such fiber-composites. This rapid fabrication and transferable sensing strategy, suitable for new and existing structures, thus provides a crosscutting SHM solution.

1. Introduction

Electrically conductive polymer composites (CPCs) generally consist of one or more polymer matrices blended with electrically conductive fillers. CPCs have been studied for decades, owing to their industrial potential for electromagnetic interference (EMI) shielding [1–3], static charge dissipation [4,5], and strain sensing [6,7]. Recent CPC-enabled strain sensing applications include body motion detection [6,8] and structural health monitoring [7,9] in the form of piezoresistive sensing [10,11]. Piezoresistive sensors operate via the change of their base electrical resistance in response to applied mechanical deformation, where sensitivity to applied strain is directly governed by the CPC's electrical resistance or conductivity [8,12].

CPC polymer matrices (thermoplastics/thermosets) are generally electrical insulators whose conductivity can be raised significantly via addition of carbon-based micro or nano conductive fillers, (e.g., graphene nanoplatelets [13–15], carbon black [16,17], carbon nanotubes [18–21]), or metallic particles (e.g., silver particles [22,23] or silver coated nanofibers [24]). Various methods of filler integration into thermoplastics have been reported, including solution casting [25], melt-mixing [26], and *in situ* polymerization [27]. Melt-mixing is preferred, as it is environmentally friendly, (i.e., solvent free), and relatively easy to scale for industrial production [28]. Nevertheless, achieving high electrical conductivity in CPCs without significant detriment to mechanical properties, processing flexibility, and cost is challenging [29]. Compared to carbon materials, superior electrical

* Corresponding authors.
E-mail addresses: jfpatric@ncsu.edu (J.F. Patrick), daniel.therriault@polymtl.ca (D. Therriault).

https://doi.org/10.1016/j.compscitech.2022.109850
Received 2 November 2022; Received in revised form 14 November 2022; Accepted 16 November 2022
Available online 23 November 2022

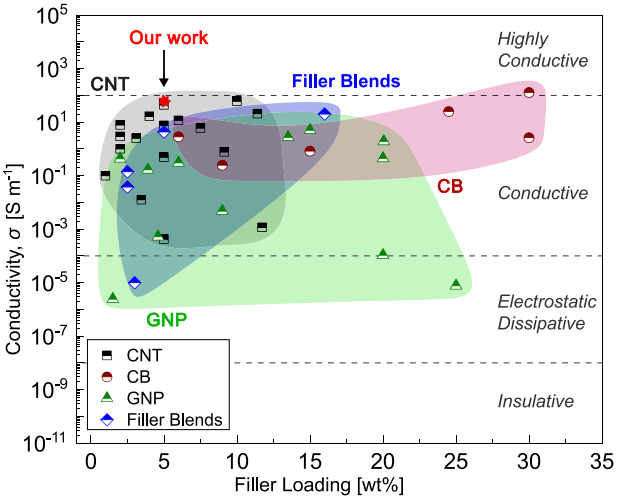

Fig. 1. Property map for melt-mixed CPC electrical conductivity per weight loading of carbon-based fillers: carbon nanotubes (CNT), carbon black (CB), graphene nanoplatelets (GNP) and blends thereof. Details for each data point and the associated literature reference are provided in Table S1.

conductivities (i.e., > 2.1×10^5 S m^{-1}) can be obtained using metallic fillers [30]. However, metal-filled composites require higher filler loadings (> 50 wt% or > 10 vol%) to reach comparable conductivity values, which results in poor processability thereby impeding their use in many applications [31].

Fig. 1 illustrates the range of CPC electrical conductivities achieved to date via melt-mixing polymer matrices with different carbon-based fillers: carbon nanotubes (CNTs), carbon black (CB), graphene nanoplatelets (GNP), or a blend of fillers. Electrical conductivities exceeding 100 S m^{-1} have proven difficult to realize, especially for CB and GNP due to their low aspect ratios (i.e., length/diameter: L/D) [4] and thus limited potential to form physical networks without high loading percentages. Electrical percolation thresholds of up to 30 wt% have been reported for carbon black, thus requiring a significant proportion of fillers to transform the polymer host from an insulator to a CPC [4,32]. Conversely, CPCs with high aspect ratio fillers ($L/D \geq 100$), i.e., multi-walled carbon nanotubes (MWCNT), typically have lower percolation thresholds and higher electrical conductivities (for a given loading) due to their ability to form a more extensive physical network [33].

Melt-mixing of MWCNT with different thermoplastic matrices has been reported, including polylactic acid (PLA) [34], polystyrene (PS) [2], polypropylene (PP) [35], polycarbonate (PC) [36], polyvinylidene fluoride (PVDF) [36], and low density polyethylene (LDPE) [37]. Additionally, the use of immiscible polymer blends as a matrix has enabled high conductivity at relatively low MWCNT loadings via selective filler segregation and overall reduction in percolation thresholds [1,22,38]. PLA/PP polymer blends have been fabricated through melt-mixing and compression to achieve ≈ 10 S m^{-1} conductivity at 10 wt% MWCNT loading [39]. Polyethylene terephthalate (PET) and LDPE blends melt-mixed with 5 wt% MWCNT have only shown conductivity up to 1 S m^{-1} [40]. Studies of CPCs using alternative copolymer matrices including poly(ethylene-co-methacrylic acid) (EMAA), to date, are limited. EMAA has commercial presence as a packaging material due to chemical resistance and excellent adhesion [41], in addition to favorable processing properties, i.e., low melt viscosity. One study of pyridine-modified EMAA melt-mixed with MWCNT showed a relatively low percolation threshold of 1.9 wt%, but exhibited an electrical conductivity of only 2.85×10^{-4} S m^{-1} [42].

The electrical conductivity of melt-mixed MWCNT CPCs can be affected by the matrix microstructure, filler formation (e.g., dispersion, distribution, and orientation), and filler–matrix interactions [25,43]. Melt-mixing process parameters such as screw speed [34], mixing time [44] and temperature [45] have exhibited a direct influence on the filler physical network formed and thus the resulting electrical properties of the CPCs produced. Increasing mixing speed and mixing time has shown more uniform MWCNT dispersion, but with variable outcomes for CPC electrical conductivity [44]. Several studies have correlated uniform MWCNT dispersion to poor electrical conductivity as a result of reduced aggregation and a less percolated MWCNT network [46,47]. Additionally, it has been reported that an increase in the mixing temperature can surpass an order of magnitude increase in electrical conductivity [48]. Thus, careful selection of melt-mixing parameters is required to obtain high electrical conductivity in CPCs, especially when considering the resulting mechanical and rheological properties of the material for further processing and end-use (e.g., printed sensors).

Interest in additive manufacturing (AM) for the fabrication of CPC strain sensing elements is rising [49,50]. While possibly forming the foundation of future manufacturing owing to design customization [51], AM techniques are reliant on mechanical and rheological property tuning of the material being deposited. Most reported studies of CPC AM are based on direct ink writing (DIW) methods [49,50,52], utilizing colloidal conductive thermoset inks that require additional curing steps. Fused filament fabrication (FFF) based on extrusion of molten thermoplastic feedstock through a nozzle is the most common AM technique today and well-suited for printing melt-mixed CPCs. FFF, however, is susceptible to variation in CPC melt viscosity and increasing the filler content often has detrimental effects on the printability. A recent study reports 3D printing of PLA/CNT into strain sensors with an electrical conductivity of ≈ 150 S m^{-1} at 12 wt%, however, a solution dispersion step is required prior to melt-mixing [53]. Another study reveals printing of melt-mixed polybutylene terephthalate (PBT)/MWCNT into a 3D structure, with a reported conductivity of 10 S m^{-1} at ≈ 11 wt% loading [54]. While the mechanical properties of CNT-loaded EMAA have been evaluated [55], no prior work has explored developing an electrically conductive, 3D-printable EMAA copolymer with strain sensing capabilities.

Here, we detail the development of a high electrical conductivity (> 40 S m^{-1}) and 3D-printable CPC by incorporating MWCNT nanofillers into an EMAA matrix via a tailored melt-mixing process. A parametric study of the melt-mixing parameters (zone temperatures, screw speed, and mixing time) at 5 wt% MWCNT loading is presented with respect to the dispersion states of MWCNT and resulting effects on electrical conductivity. Then, EMAA CPC with various MWCNT loadings (0.5–10 wt%) are produced and the percolation threshold, rheological properties, and printability are investigated. The CPC with the best printability/conductivity is 3D printed onto a glass fiber-reinforced polymer (GFRP) composite and repeatable flexural sensing is demonstrated. This work showcases the use of solely melt-mixing to produce a CPC with high electrical conductivity at low enough MWCNT loading to 3D print a functional, reliable piezoresistive strain sensor.

2. Experimental

2.1. Materials

Nucrel 2940™ (DuPont Inc., USA) EMAA copolymer is used as-received, with a density of 0.944 g cc^{-1} and melt flow index of 395 g/10 min at 190 °C [56]. Multi-walled carbon nanotubes (NC7000, Nanocyl™, Belgium) produced via Catalytic Chemical Vapor Deposition [57], are used as-received. The MWCNT possess an average diameter of 9.5 nm, average length of 1.5 μm, surface area of 250–300 m^2 g^{-1}, electrical conductivity of 10^3–10^5 S m^{-1} and reported density of 1.75 kg m^{-3} [58,59]. Eight harness (8H) satin weave style 7781 E-glass (Hexcel, Inc., USA) is used in conjunction with an epoxy resin system (Araldite 8605LY/Aradur 8605, Huntsman Advanced Materials, LLC, USA) to fabricate the GFRP flexure samples for the strain sensing demonstration. Canada balsam (Alfa Aesar, USA) is used as the mounting medium for microtomy samples. Epoxy resin and hardener (EpoxyCure 2, Buehler, USA) are used as the embedding medium for microtomy samples.

Table 1
Melt-mixing conditions for the parametric study of EMAA-CNT(5 wt%) by varying: zone three barrel temperature (T_3), screw speed (υ), and mixing time (t).

Study	Temperature ($T_1/T_2/T_3$) [°C]	Screw speed υ [rpm]	Mixing time t [min]
Effect of T_3	120/150/**160** 120/150/**180** 120/150/**200** 120/150/**220** 120/150/**240**	200	5
Effect of υ	120/150/200	**25** **50** **100** **200** **400**	5
Effect of t	120/150/200	50	**3** **5** **7** **9**

Table 2
Melt-mixing conditions for EMAA CPCs at different MWCNT loadings. Varied zone temperatures are shown for a fixed screw speed (50 rpm) and mixing time (5 min).

Samples	Temperature ($T_1/T_2/T_3$) [°C]
Neat EMAA	80/120/**120**
EMAA-CNT(0.5 wt%)	80/120/**130**
EMAA-CNT(1 wt%)	80/120/**130**
EMAA-CNT(2 wt%)	80/120/**150**
EMAA-CNT(3 wt%)	80/120/**170**
EMAA-CNT(5 wt%)	120/150/**200**
EMAA-CNT(7 wt%)	120/150/**220**
EMAA-CNT(9 wt%)	120/150/**240**

2.2. CPC preparation

EMAA pellets and MWCNT are weighed and physically combined as-received. Melt-mixing is performed using a co-rotating micro twin-screw extruder (DSM Xplore MC5, Netherlands) with three distinct heating zones: $T_1/T_2/T_3$ (see equipment schematic in Fig. S1). A preliminary screening based on manufacturer technical data was performed, which confirmed the need for barrel zone temperatures ($T_1/T_2/T_3$) of at least 120/150/180 °C with screw speed (υ) = 50 rpm and mixing time (t) = 5 min, achieving an electrical conductivity > 10 S m^{-1} in melt-mixed CPCs at 5 wt% MWCNT loading. This pre-screening formed the basis for a subsequent parametric study of CPC electrical conductivity as a function of melt-mixing processing parameters (T, υ, t) at 5 wt% MWCNT loading. In the parametric study, EMAA-CNT(5 wt%) is melt-mixed at a constant T_1/T_2 = 120/150 °C, while varying T_3 (160 °C–240 °C), υ (25–400 rpm), and t (3–9 min) as shown in Table 1.

CPCs with varying MWCNT loadings (0.5–9 wt%) are also prepared at constant υ (50 rpm) and t (5 min), respectively. For 2 wt% and above, the zone 2 and 3 barrel temperatures (i.e., T_2 and T_3) are increased in accordance with the MWCNT loading (see Table 2) to offset the nanofiller-induced viscosity increase of the polymer melt and maintain a mixing shear force between 400–500 N (see Table S3). Extruded CPC filaments for 5 wt% and above are air-cooled, but extruded filaments with lower MWCNT loadings are water-cooled to retain filament shape since melt viscosities are relatively low. The extruded CPC filaments (1.70–2.00 mm in diameter) are further characterized and used as the feedstock for 3D printing of strain sensors.

2.3. Characterization

2.3.1. Electrical conductivity

The electrical conductivity of the extruded CPC filaments is measured using the four-point probe method. Silver ink (Super Shield, USA) is applied to negate wire and contact resistance [60] on four electrode points spaced 1.25 mm apart on 5 cm long filaments (see Fig. S2a). An electrical current (I) is applied on the two outer electrodes using a current source (6221, Keithley Instruments, USA) while the voltage difference (V) is measured using a nanovoltmeter (2182 A, Keithley Instruments, USA) on the two inner electrodes. The resistance (R) is then calculated from the slope of the I-V curve (voltage on the y-axis) and the conductivity (σ) defined as:

$$\sigma = \frac{1}{\rho} = \frac{1}{R}\frac{4l}{\pi d^2} \quad (1)$$

where ρ is the resistivity, l is the distance between electrodes and d is the diameter of the filament. The instruments employed for the four-point probe method are configured for low resistance CPCs (1 Ω–1 kΩ). CPCs with higher resistance (i.e., >1 kΩ) are measured using the two-point probe method due to resistive heating and localized melting occurring during four-point probe measurements. For the two-point probe measurements, CPC filaments are placed within a Faraday cage (see Fig. S2b) that is connected to an electrometer (6517B, Keithley Instruments, USA) to shield from external electrical fields and obtain accurate measurements.

2.3.2. MWCNT micro- and nano-dispersions

To investigate the effect of melt-mixing parameters on the micro-dispersions of MWCNT within the extruded CPC filaments, cryo-microtomy (RM2165 with cryo-chamber, Leica Microsystems GmbH, Germany) is performed. Prior to microtomy, the CPC filaments are embedded within epoxy resin using flat silicone molds (70 903, EMS, USA). Thin sectioning (5 μm) is performed on the surface parallel to the filament cross-section at −15 °C. The sections are then mounted on glass slides using Canada balsam. The cross-sections are subsequently imaged via optical microscopy (BX-61, Olympus, Japan) with a 5 MP camera (C-P3 Optika Microscopes, Italy). Images are post-processed in ImageJ (NIH, USA) to determine the MWCNT aggregate area ratio ($r_a = A_a/A_o$), where A_a is the area of MWCNT aggregates with size larger than 10 μm and A_o is the total investigated area (A_o >1.5 mm^2 per section) [61]. For each sample set, at least 6 sections are obtained from two different locations along the filament.

To study the nano-dispersion state of the MWCNT, CPC sections are observed using transmission electron microscopy (TEM) (JEM-2100F, JEOL, USA) at 200 kV. The 70–100 nm thin sections are obtained from an ultra-microtome (EM UC7, Leica Microsystems GmbH, Germany) at −25 °C and deposited on TEM holder grids (copper, 400 mesh) prior to imaging.

2.3.3. Rheology

The neat EMAA and CPCs produced from melt-mixing are pelletized and compression molded with 33 kN of piston force in a nitrogen environment at temperatures between 180–240 °C according to the MWCNT loading (see Table S4) to produce 25 mm diameter disks 1.5 mm thick. Rheological characterization is performed via small amplitude oscillatory shear (SAOS) experiments in a nitrogen environment using a rheometer (MCR302, Anton Paar, Austria) with a 25 mm parallel plate geometry and 1 mm gap. Amplitude sweeps are performed to determine the linear viscoelastic (LVE) region of each CPC under applied strains 0.5–50% and angular frequency of 10 rad s^{-1} at 190 °C. Frequency sweep tests are then conducted for each sample from 0.1 to 100 rad s^{-1} within the determined LVE range at 190 °C.

2.3.4. Fabrication of GFRP composite flexure substrates for strain sensing

Composite preforms are prepared by stacking twelve woven plies of 8H satin E-glass in an alternating sequence of $[0/90]_6$, where [0] indicates the warp direction and [90] is the weft direction. The preforms are infused via the vacuum-assisted resin transfer molding (VARTM) process. Infiltration of liquid epoxy resin and amine hardener (mixed 100:35 by weight) occurs at 2 Torr (abs) until complete fabric wetting

and then vacuum is decreased to 380 Torr (abs) for 24 h at room temperature until matrix solidification. The composite panels are cured for 2 hr at 121 °C followed by 2 hr at 150 °C. Samples 13 mm wide and 84 mm long are cut from the ≈ 2.8 mm thick cured composite using a diamond-blade wet saw. The flexural samples are prepared for digital image correlation (DIC) by spray-painting the front profile (2.8 mm thick × 84 mm long) matte white followed by speckling with matte black paint to produce a high-contrast pattern.

2.3.5. 3D-printing of EMAA-MWCNT strain sensors

Using EMAA-CNT(5 wt%) CPC material as feedstock, sensing traces roughly 150 μm thick by 750 μm wide are deposited via fused filament fabrication (LulzBot TAZ Pro) onto GFRP sample substrates using a 0.8 mm diameter nozzle at a temperature of 190 °C and a bed temperature of 60 °C. A continuous serpentine pattern, comprising five segments (10 mm long) spaced 2.75 mm apart, is printed at the center of the top face on each sample. The two end-points of the serpentine pattern are connected to 0.65 mm diameter copper wire using silver paint (Ted Pella Inc., USA), and the connections are coated with a thin layer of structural adhesive (DP460 NS, 3M Inc., USA) to ensure resilience during mechanical cycling.

2.3.6. Flexure testing of GFRP substrates with 3D-printed strain sensors

GFRP beam samples are tested within elastic strain limits in a 3-point flexure configuration using a 10 kN electromechanical load frame (RT/5, MTS, Inc., USA). A span to depth ratio of 32:1 is selected to reduce shear effects, in accordance with ASTM D7264. Samples are preloaded to 5 N, which ensures sufficient loading pin contact with the substrate, and then tested at a crosshead rate of 1 mm min^{-1} for 20 consecutive load–unload cycles at 0.4% and 0.8% maximum flexural strain for the first and last decade, respectively. Load and crosshead displacement data are collected at a sampling rate of 5 Hz throughout the process. Concurrent images of the speckled front sample face are acquired using a 12.3 MP camera (GS-3-U3-15S5C-C, Teledyne FLIR, Inc., USA) to capture the full-field displacements for digital image correlation (DIC). Time-stamped images are analyzed using DIC software (VIC-2D, Correlated Solutions, Inc.) to calculate the maximum flexural strains on the bottom (i.e., tensile) face of the composite substrate. Piezoresistive sensor data is concurrently collected at a sampling rate of 1 Hz using a digital multimeter (DMM) (Model 7510, Tektronix, Inc., USA) connected in a four-point probe configuration, (i.e., two separate contact points to each of the two copper wires emanating from each serpentine sensor).

3. Results and discussion

3.1. Melt-mixing screening and parametric studies of EMAA-CNT(5 wt%)

The preliminary screening based on prior literature [48] confirms that higher barrel temperatures during melt-mixing result in greater electrical conductivity for EMAA-CNT(5 wt%). These findings motivated a subsequent parametric study, varying the screw speed (υ), mixing time (t), and barrel temperature in the third zone (T_3) where T_1 and T_2 are held constant at 120 °C and 150 °C, respectively.

The first parameter varied is T_3, from 160 to 240 °C in 20 °C increments, with a constant υ = 200 rpm and t = 5 min. Fig. 2a shows that increasing the final zone 3 barrel temperature (T_3) enhances electrical conductivity from 9.4 S m^{-1} at 160 °C to 41.1 S m^{-1} at 220 °C, while a decrease in conductivity to 31.2 S m^{-1} occurs when T_3 is increased further to 240 °C. Temperature sweep rheological studies (see Fig. S3) reveal that the viscosity of neat EMAA decreases with increasing temperature until 228 °C, rising rapidly thereafter. The increased viscosity (accompanied by increased mixing force) indicates the onset of polymer thermal degradation, where oxidation of the EMAA matrix affects the interfacial chemical bonding and electron transport between neighboring EMAA-CNT and CNT–CNT regions, likely explaining the lower conductivity at T_3 = 240 °C. MWCNT micro-dispersion studies at three different temperatures (T_3 = 160 °C, 200 °C and 240 °C) are performed and the calculated MWCNT aggregate area ratios (r_a), are plotted in Fig. 2a(i) for respective microscopic images in Fig. 2a(ii-iv). No clear trend is observed between T_3 and r_a, where the low values of r_a < 5% could be due to the relatively high mixing speed (υ = 200 rpm), which facilitates the diffusion of polymer chains into MWCNT aggregates.

In a subsequent investigation, the screw speed is now varied (25, 50, 100, 200 and 400 rpm) with constant t = 5 min and T_3 = 200 °C. As shown in Fig. 2b(i), lower screw speeds (25, 50 rpm) correlate to higher r_a (5–13%) and electrical conductivity (36–44 S m^{-1}). However, the effect of screw speed on conductivity appears insignificant after 100 rpm. Higher conductivities achieved at screw speeds of 25/50 rpm are also reported in the melt-mixing studies of polyamide and poly(caprolactone) MWCNT-based composites [35,44]. As determined from cryo-microtomy, the aggregate area ratio decreases from 12% to less than 2% as screw speed is increased from 25 rpm to 400 rpm, correlating to reduction in MWCNT aggregation shown in Fig. 2b(ii-iv). No firm trend seems to exist between the electrical conductivity and aggregate ratio r_a.

Varying the final parameter, mixing time (i.e., 3, 5, 7, 9 min), while holding constant T_3 = 200 °C and υ = 50 rpm reveals that a melt-mixing duration of 5 min maximizes the EMAA-CNT(5 wt%) electrical conductivity (Fig. 2c) reaching a value of 43.9 S m^{-1}. Longer mixing time beyond 5 min results in lower conductivity while r_a increases, possibly due to secondary agglomeration, which is supported by existing literature [35,47]. This parametric study reveals that zone three barrel temperature, screw speed, and mixing time all influence the electrical conductivity of EMAA-CNT(5 wt%). The process parameters that achieve the highest conductivity are: T_3 = 220 °C, υ = 50 rpm, and t = 5 min. The optimal screw speed (υ = 50 rpm) and mixing time (t = 5 min) for 5 wt% MWCNT are subsequently used to investigate melt-mixing of CPCs at different filler percentages. The barrel temperature profile is adjusted relative to MWCNT loading (see Table 2) to limit the applied shear force on the melt and prevent MWCNT diffusion/breakage that could reduce the electrical conductivity of the CPC [35].

3.2. Electrical properties

Fig. 3a compares the electrical conductivity of neat EMAA and CPCs for varying MWCNT loadings (0.5–10 wt%) produced using melt-mixing parameters from the preliminary screening versus those gained from the parametric study. For the CPCs produced with the selected (υ = 50 rpm, t = 5 min) parameter set, the percolation threshold, (ϕ_c), determined from a power-law curve fit (see Fig. S4) is ≈ 1.7 wt% (≈ 1.0 vol%). Above the ϕ_c, we observe a significant increase in measured electrical conductivity due to the formation of a three dimensional conductive network via the direct physical interactions of MWCNT. The percolation threshold for EMAA/CNT is similar to a reported value for LDPE/MWCNT (ϕ_c ≈ 1.5 wt%), however, the measured conductivity (≈ 1.0 S m^{-1}) at 5 wt% is nearly forty times lower than our result (43.9 S m^{-1}) at the same loading [37]. This also compares favorably to recent EMAA-CNT nanocomposites, which have reported conductivities of less than 10 S m^{-1} at 7 wt% MWCNT loading [62].

The electrical conductivities of EMAA/MWCNT CPCs herein, mixed at lower temperatures (i.e., the preliminary screening), are significantly lower with higher ϕ_c ≈ 4.0 wt% than those mixed at higher temperatures. A possible factor contributing to the lower measured conductivities is poor adsorption of EMAA polymer chains onto MWCNT aggregates [48], supported by observed aggregate detachment from the EMAA matrix (see Fig. S5), thereby reducing MWCNT network connectivity. The difference in electrical conductivities is magnified as MWCNT loading increases beyond 1.0 wt%. For example, at 5 wt%, the conductivity increases by five orders from 1.40 × 10^{-4} S m^{-1} to

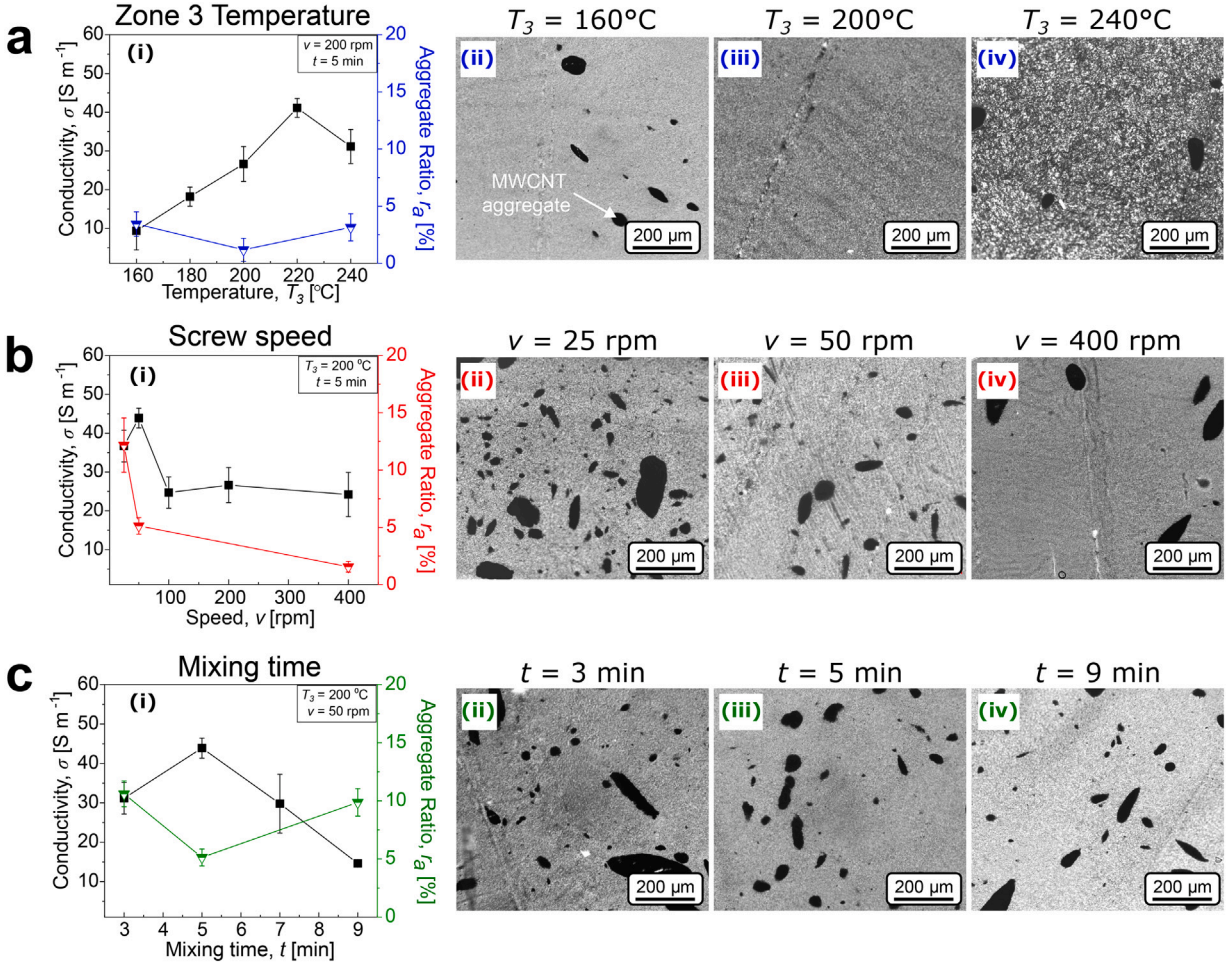

Fig. 2. Melt-mixing screening studies of EMAA-MWCNT(5 wt%) based on three different parameters; (a) zone 3 barrel temperature, T_3, (b) screw speed, v, and (c) mixing time, t. (i) Plots of electrical conductivity and aggregate area ratios ($r_a = A_a/A_o$) determined via optical microscopy (representative images ii–iv), from cryo-microtomy samples revealing the micro-dispersion states of MWCNT aggregates.

4.39×10^1 S m^{-1} when the barrel zone temperatures ($T_1/T_2/T_3$) are increased from (80/150/110 °C) to (120/150/200 °C) for the same mixing time of 5 min; screw speeds are 100 and 50 rpm, respectively. The observed increase in conductivity can be explained via images of the micro- and nano-dispersion states of MWCNT in EMAA as shown in Fig. 3(b–g). At the micro-scale, similar aggregate area ratios of 4.4% and 5.1% were calculated for both mixing profiles. However, CPCs produced at lower mixing temperatures (80/150/110 °C) contain greater numbers of smaller MWCNT aggregates, leading to lower electrical conductivity. At this lower mixing temperature profile, the viscosity of EMAA is higher (see Fig. S3), which results in greater mixing-induced shear force on the MWCNT aggregates and a higher degree of aggregate breakdown. This in-turn disentangles MWCNT bundles and produces a fairly uniform, but diluted distribution of MWCNT within the EMAA matrix [63], which leads to a poor conductive network as they become too physically distant to enable electron transport [64]. This diffuse and homogeneous distribution at the nano-scale captured via TEM (Fig. 3c–d) is markedly different than the dispersion state of MWCNT in CPCs produced by the higher mixing temperature profile. A high contrast of black (MWCNT aggregates) and white (EMAA matrix) regions reveal dense MWCNT networks with more heterogeneous nano-scale distributions (Fig. 3f–g), indicating tighter MWCNT groupings and better physical interconnections at the nano-scale. Thus, nano-scale heterogeneity with banded regions of MWCNT percolation results in higher electrical conductivity than homogeneous, yet more diffuse MWCNT distributions at the same loading.

3.3. Rheological properties

Rheological properties of the melt-mixed CPCs with varying MWCNT loadings are investigated via small amplitude oscillatory shear testing. The experimental temperature is set to a constant 190 °C, the set-point for subsequent 3D printing via FFF in order to relate the rheological behavior to the nozzle temperature during the printing process. Both the storage (G') and loss (G'') moduli increase with MWCNT loading as shown in Fig. 4(a–b). At low oscillation frequencies (0.1–10 rad s^{-1}), a roughly two order of magnitude increase in G' for CPCs relative to neat EMAA was observed at 0.5 wt% loading, and up to six orders of magnitude increase at 7 wt%. Frequency independence of G' is observed as MWCNT loading increases, especially beyond 5 wt%, indicating that the rheological properties are more representative of a solid. Such solid-like behavior is linked to the formation of MWCNT connected networks within the composites [15]. Tan (δ) corresponds to the ratio of viscous (G'') to elastic (G') response of neat EMAA and the CPCs, as shown in Fig. 4(c). The transition from liquid-like ($G'' > G'$) to solid-like ($G' > G''$) behavior occurs at 3 wt%, indicating the formation of interconnected MWCNT networks and restriction of the EMAA polymer matrix chains [65]. Thus, the rheological percolation threshold is somewhere between 1 to 3 wt%.

As shown in Fig. 4d, the complex viscosity, η^* increases with MWCNT loading, though more notably within the lower oscillation frequency range. The incorporation of MWCNT induces shear-thinning behavior in EMAA-based CPCs, whereas the neat EMAA copolymer exhibits a Newtonian response. For CPCs at low MWCNT loadings (0.5

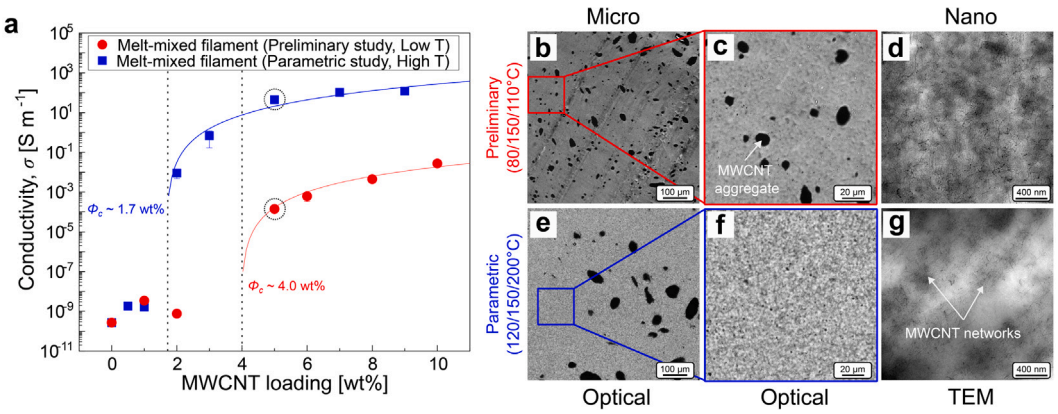

Fig. 3. (a) Electrical conductivity of EMAA CPCs with varying wt% of MWCNT from the preliminary and parametric studies, with percolation thresholds (ϕ_c) of 4.0 wt% and 1.7 wt%, respectively (each demarcated by a dashed vertical line). Complementary optical microscopy and TEM images of EMAA-CNT(5 wt%) showing micro- and nano-dispersion states of MWCNT for the preliminary (b–d) and parametric studies (e–g). Note: dashed circles indicate the data points for accompanying micrographs.

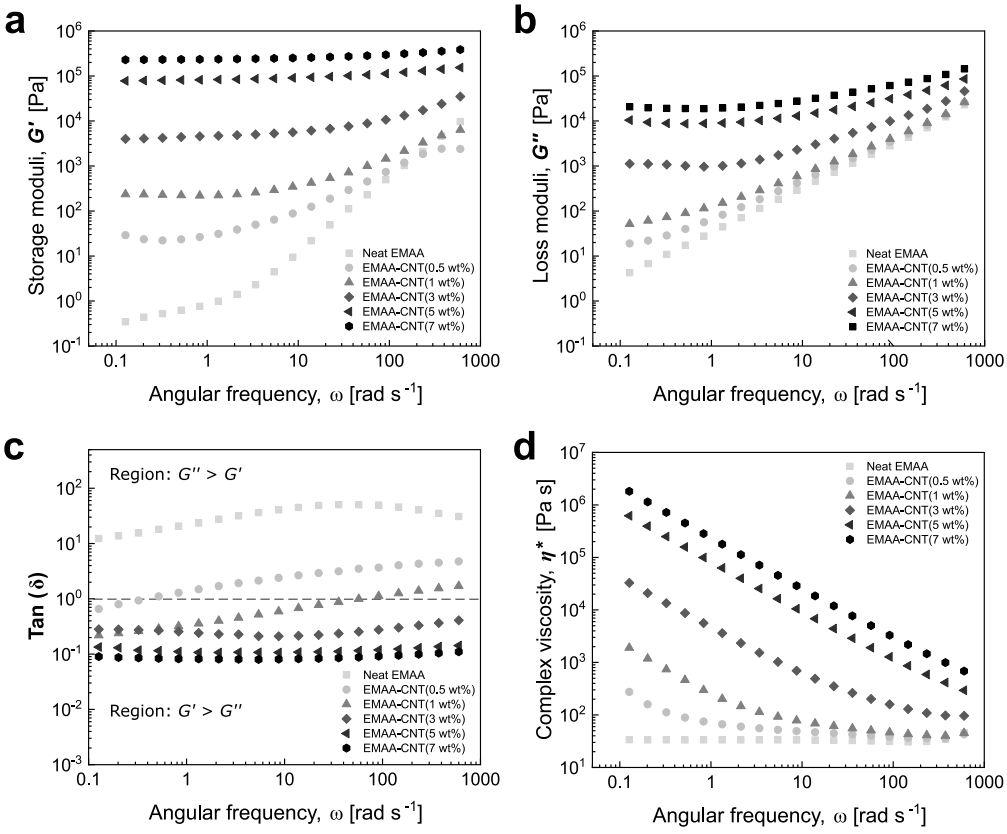

Fig. 4. Frequency sweep rheological characterization of neat EMAA and MWCNT CPCs at 190 °C. (a) Storage modulus, G', and (b) Loss modulus, G'' vs. angular frequency, (ω) obtained within the linear viscoelastic (LVE) region. (c) Tan (δ) calculated as the ratio of G'' to G'. The dashed line demarcates the transition between G'' dominated (liquid-like) and G' dominated (solid-like) behavior. (d) Complex viscosity, η^* as a function of ω.

and 1 wt%), shear-thinning is only observed at lower frequency ranges (0.1–10 rad s^{-1}). However, the degree of shear-thinning behavior is more pronounced (i.e., steeper slope) with increased MWCNT loading. Such behavior is important for additive manufacturing as it allows the molten material to flow at high shear rates during printing and maintain shape after printing [66].

3.4. Printability of EMAA-MWCNT

Extruded filaments of melt-mixed CPC are utilized as feedstock for fused-filament fabrication (FFF) and printed along linear tool-paths through a 0.8 mm diameter nozzle as shown in Fig. 5a. Linear traces of CPCs at lower MWCNT loadings (1–5 wt%) are successfully printed at a nozzle temperature (T_{nozzle}) of 190 °C and bed temperature (T_{bed}) of 60 °C, while exhibiting strong adhesion (Fig. 5b). However, due to the higher viscosity at 7 wt% MWCNT loading, a higher T_{nozzle} = 210 °C is required for printing, but nonetheless exhibits increased waviness. Even with a nozzle temperature beyond 210 °C (but below the EMAA thermal degradation temperature ~ 230 °C), printing of the EMAA-CNT(9 wt%) material is not viable due to intermittent nozzle clogging and resulting discontinuous printed traces. In general, the print quality (i.e., dimensional control) decreases and the surface roughness and macro-waviness increase with greater MWCNT loading.

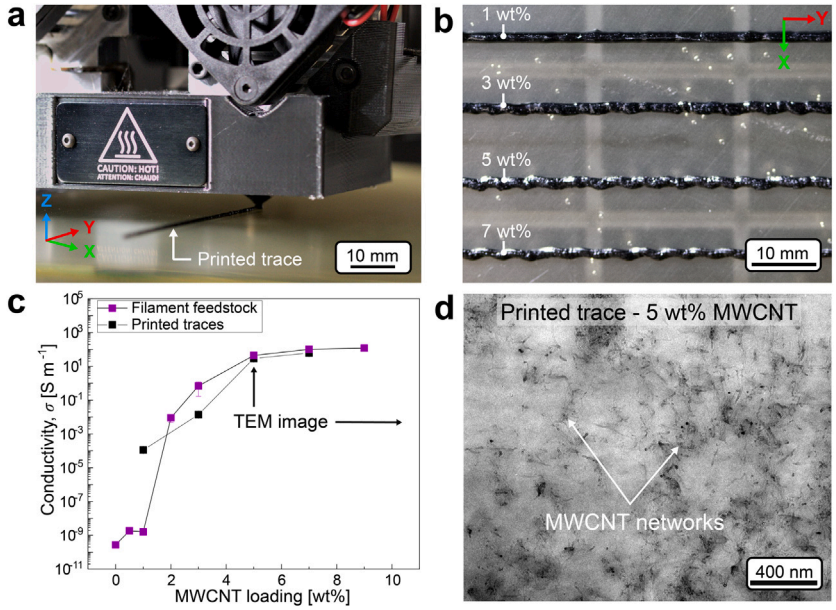

Fig. 5. 3D printing study via FFF of EMAA/MWCNT CPCs. (a) Nozzle melt-extrusion along a linear toolpath. (b) Printed traces of EMAA-CNT at 1, 3, 5 and 7 wt% MWCNT loading. (c) Electrical conductivities of pre-print filament feedstock and post-print traces at various MWCNT loadings. (d) TEM image of 5 wt% MWCNT printed trace.

In Fig. 5c, the electrical conductivities of printed traces measured via the four-point probe method using a digital multimeter (DMM) are shown in comparison to the base feedstock. At low MWCNT loadings (1 and 3 wt%), the post-print conductivities vary widely from the pre-print measurements. However, at higher MWCNT loadings the pre- versus post-print conductivity values are of the same order: 43.9 S m^{-1} vs. 29.3 S m^{-1} at 5 wt% and 101.7 S m^{-1} vs. 61.6 S m^{-1} at 7 wt%. The retention of high electrical conductivity after printing for the EMAA-CNT(5 wt%) material is explained by the TEM image in Fig. 5d, revealing the preservation of heterogeneous MWCNT dispersions and connected networks even after the FFF process. EMAA-CNT(5 wt%) was selected for subsequent investigation of 3D printed flexural strain sensing owing to its printability and maintained electrical conductivity.

3.5. Strain sensing demonstration

FFF of EMAA-CNT(5 wt%) produces viable piezoresistive sensing capability that is demonstrated by a strain sensor printed on the tensile face of a GFRP composite and tested under cyclic 3-point flexure (see Fig. 6). Continuous monitoring of sensor resistance is achieved via four-point probe using the DMM connected to the copper wire electrodes embedded into the printed sensors. The sensor design comprises a continuous serpentine trace with a target line width of 750 μm and target thickness of 150 μm (see Fig. 6b,c). The 150 μm thickness is the minimum printable single layer thickness possible on the FFF equipment utilized. Printing at these cross-sectional dimensions keeps the sensor resistance within the 10–100 kΩ range, well within the operating window of the DMM (1 Ω–1 GΩ). Printing below this thickness often results in notable sensor resistance increase due to defects induced by GFRP substrate undulations, which are on the order of 100 μm peak-to-valley surface roughness [67]. The well-documented and advantageous reactivity between EMAA and the diglicidyl ether of bisphenol A (DGEBA) epoxy matrix of the GFRP [68–70] enables strong adhesion between the substrate and printed sensor, thus ensuring surface strain coupling. The serpentine sensor is designed to encompass the entire width of the GFRP beam (13 mm) and spans a 10 mm central portion along the length.

Evaluation of the flexural piezoresistive response of the nanocomposite sensor is conducted within the tensile elastic strain limit of the underlying GFRP substrate (≤ 0.8%). To assess the sensitivity of the printed CPC across a wider strain range, testing is conducted at both 0.4% and 0.8% maximum applied flexural strain on the bottom (tensile) face of the substrate opposite and verified by digital image correlation (DIC). The two values of maximum strain are applied for 10 consecutive load–unload cycles (Fig. 6d), with the sensor resistance measured and recorded throughout. For each test cycle, the peak strain and maximum measured resistance align directly in time, indicating no delay in sensor response at the crosshead displacement rate tested (1 mm min^{-1}). Sensor resistance increases slightly through the first few successive cycles at a given strain range and then converges, indicative of mechanically-induced physical changes to the MWCNT networks prior to reaching an equilibrium configuration.

This behavior is also apparent from the relative change in sensor resistance to initial resistance ($\Delta R/R_0$) as shown in Fig. 6e. While sensitivity reduces slightly after the first respective cycle for each strain level (1st 0.4%, 11th 0.8%), the response quickly converges and remains consistent in each case with low hysteresis and no sign of sensor degradation. This indicates a positive prognosis for longer-term sensing applications beyond the 20 cycles conducted herein, which were taken to be a reasonable threshold value for proving repeatable functionality based on convergent sensor behavior.

4. Conclusion

In this work, an electrically conductive nanocomposite comprising an EMAA copolymer matrix and MWCNT fillers has been developed via melt-mixing for readily accessible 3D printing. A parametric study to elucidate the dominant mixing parameters results in a conductive polymer exceeding 40 S m^{-1} at only 5 wt% MWCNT loading, one of the highest values achieved to date at this filler content. Reaching appreciable electrical conductivity while maintaining printability (i.e., low melt-viscosity) is predicated upon the formation of a heterogeneous MWCNT nano-scale distribution that is preserved after fused-filament fabrication. Printing EMAA-CNT(5 wt%) onto a glass–fiber composite in a serpentine pattern produces a well-adhered flexural strain sensor with robust piezoresistive performance over 20 consecutive test cycles featuring low hysteresis and no indication of sensor degradation for elastic deformation of the underlying composite. When paired with geometric design agility offered by FFF additive manufacturing, for both flat and curved surfaces [71], this emergent nanomaterial holds

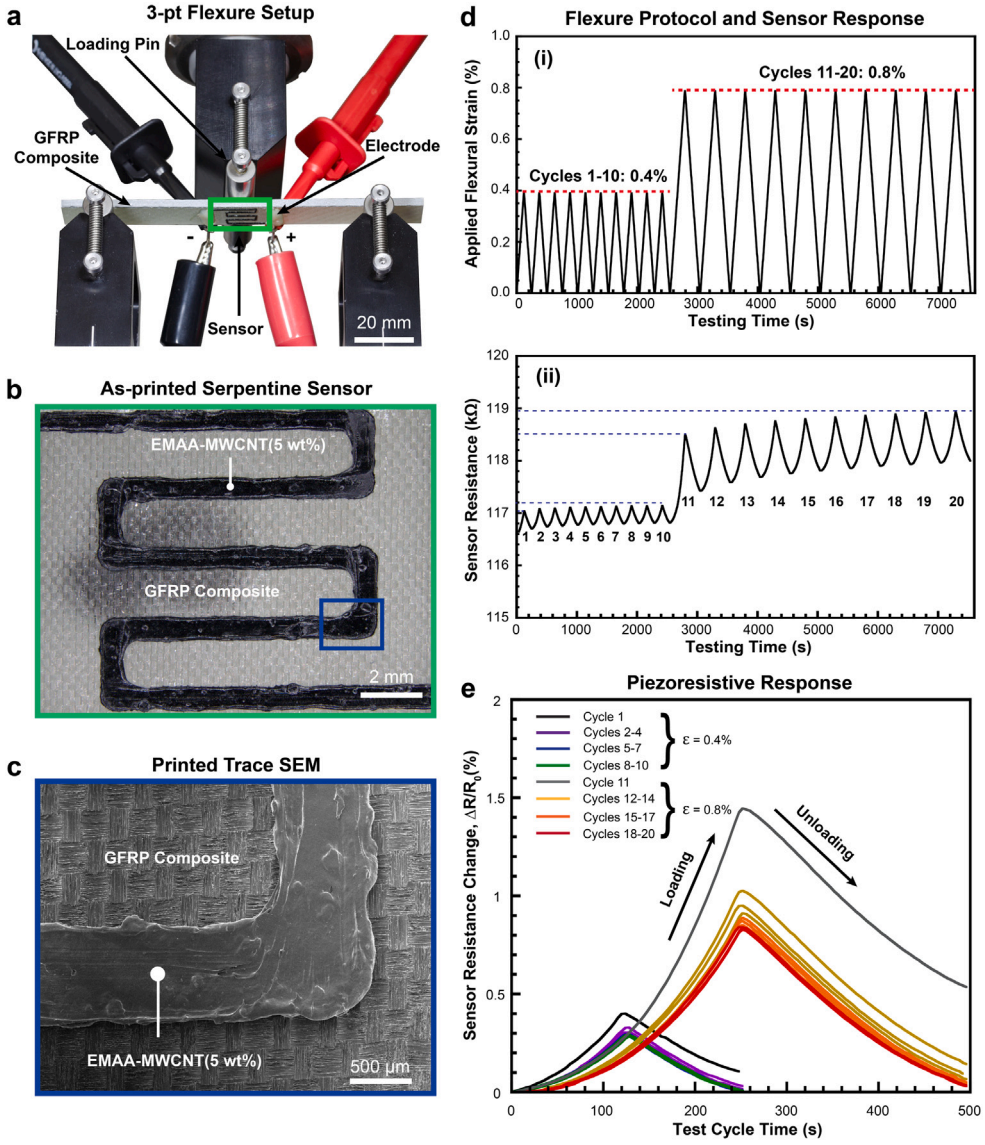

Fig. 6. Strain sensing of 3D-printed EMAA-CNT(5 wt%). (a) 3-point flexural test configuration showing printed sensor and electrode locations. Optical micrograph (b) and scanning electron micrograph (SEM) (c) of as-printed serpentine sensor on GFRP substrate. (d) Applied flexural strains (i) for 20 consecutive test cycles (10 at 0.4%, 10 at 0.8%) measured via DIC. Piezoresistive response (ii) for the applied strains at individual test cycles. (e) Relative change in sensor resistance ($\Delta R/R_0$) for each test cycle (1–20).

promise as a transferable SHM solution for new and existing composite infrastructure. Immediate opportunity has been created to study alternative sensor designs and extended cycling under various loading scenarios and environmental conditions. Further implements will explore the suitability of this multifunctional material for electromagnetic interference (EMI) shielding [72], thermo-mechanical actuation [73] and energy harvesting [74].

CRediT authorship contribution statement

Iee Lee Hia: Investigation, Formal analysis, Writing – original draft, Writing – review & editing, Visualization. **Alexander D. Snyder:** Investigation, Formal analysis, Writing – original draft, Writing – review & editing, Visualization. **Jack S. Turicek:** Investigation, Formal analysis. **Fernanda Blanc:** Investigation. **Jason F. Patrick:** Conceptualization, Methodology, Resources, Writing – review & editing, Visualization, Supervision, Project administration, Funding acquisition. **Daniel Therriault:** Conceptualization, Methodology, Resources, Writing – review & editing, Visualization, Supervision, Project administration, Funding acquisition.

Declaration of competing interest

The authors declare that they have no known competing financial interests or personal relationships that could have appeared to influence the work reported in this paper.

Data availability

Data will be made available on request.

Acknowledgments

The authors would like to acknowledge the financial support from the Natural Sciences and Engineering Research Council (NSERC) through grant No. CRDPJ 514761-1 awarded to D.T., Quebec Research Fund and Canada Foundation for Innovation (CFI), Canada. This work has also been partially supported by the Strategic Environmental Research and Development Program (SERDP), USA through grant No. W912HQ21C0044 awarded to J.F.P. The work was performed in part at the Analytical Instrumentation Facility (AIF) at North Carolina

State University, which is supported by the State of North Carolina and the National Science Foundation, USA (grant ECCS-2025064). We would also like to thank Mr. Matthieu Gauthier, Ms. Claire Cerclé and Mr. Jean-Philippe Masse for the training and measurements provided in rheological, microtomy, SEM and TEM characterization. We are grateful to Mr. Yanik Landry-Ducharme, Dr. Jose Martinez, Dr. Paulina Latko-Durałek, Dr. Kambiz Chizari, Dr. Petra Pötschke and Prof. Jason Robert Tavares for their advice on the respective electrical conductivity, MWCNT dispersion and cryo-microtomy subject areas.

Appendix A. Supplementary data

Supplementary material related to this article can be found online at https://doi.org/10.1016/j.compscitech.2022.109850.

References

[1] S.N. Sultana, S.P. Pawar, U. Sundararaj, Effect of processing techniques on EMI SE of immiscible PS/PMMA blends containing MWCNT: enhanced intertube and interphase scattering, Ind. Eng. Chem. Res. 58 (26) (2019) 11576–11584.
[2] J.P.S. da Silva, B.G. Soares, S. Livi, G.M. Barra, Phosphonium–based ionic liquid as dispersing agent for MWCNT in melt-mixing polystyrene blends: Rheology, electrical properties and EMI shielding effectiveness, Mater. Chem. Phys. 189 (2017) 162–168.
[3] K. Chizari, M. Arjmand, Z. Liu, U. Sundararaj, D. Therriault, Three-dimensional printing of highly conductive polymer nanocomposites for EMI shielding applications, Mater. Today Commun. 11 (2017) 112–118.
[4] T.F.d. Silva, F. Menezes, L.S. Montagna, A.P. Lemes, F.R. Passador, Preparation and characterization of antistatic packaging for electronic components based on poly(lactic acid)/carbon black composites, J. Appl. Polym. Sci. 136 (13) (2019) 47273.
[5] F. Doğan, K. Şirin, F. Kolcu, İ. Kaya, Conducting polymer composites based on LDPE doped with poly (aminonaphthol sulfonic acid), J. Electrost. 94 (2018) 85–93.
[6] Y. Wang, L. Wang, T. Yang, X. Li, X. Zang, M. Zhu, K. Wang, D. Wu, H. Zhu, Wearable and highly sensitive graphene strain sensors for human motion monitoring, Adv. Funct. Mater. 24 (29) (2014) 4666–4670.
[7] J.-W. Zha, B. Zhang, R.K. Li, Z.-M. Dang, High-performance strain sensors based on functionalized graphene nanoplates for damage monitoring, Compos. Sci. Technol. 123 (2016) 32–38.
[8] M. Amjadi, A. Pichitpajongkit, S. Lee, S. Ryu, I. Park, Highly stretchable and sensitive strain sensor based on silver nanowire–elastomer nanocomposite, ACS Nano 8 (5) (2014) 5154–5163.
[9] C. Li, T.-W. Chou, Modeling of damage sensing in fiber composites using carbon nanotube networks, Compos. Sci. Technol. 68 (15–16) (2008) 3373–3379.
[10] N. Hu, H. Fukunaga, S. Atobe, Y. Liu, J. Li, Piezoresistive strain sensors made from carbon nanotubes based polymer nanocomposites, Sensors 11 (11) (2011) 10691–10723.
[11] Y. Yang, W. Guo, J. Qi, Y. Zhang, Flexible piezoresistive strain sensor based on single sb-doped ZnO nanobelts, Appl. Phys. Lett. 97 (22) (2010) 223107.
[12] X. Liu, X. Liang, Z. Lin, Z. Lei, Y. Xiong, Y. Hu, P. Zhu, R. Sun, C.-P. Wong, Highly sensitive and stretchable strain sensor based on a synergistic hybrid conductive network, ACS Appl. Mater. Interfaces 12 (37) (2020) 42420–42429.
[13] M. Li, C. Gao, H. Hu, Z. Zhao, Electrical conductivity of thermally reduced graphene oxide/polymer composites with a segregated structure, Carbon 65 (2013) 371–373.
[14] Z. Liu, D. Shen, J. Yu, W. Dai, C. Li, S. Du, N. Jiang, H. Li, C.-T. Lin, Exceptionally high thermal and electrical conductivity of three-dimensional graphene-foam-based polymer composites, RSC Adv. 6 (27) (2016) 22364–22369.
[15] Y. Tan, L. Fang, J. Xiao, Y. Song, Q. Zheng, Grafting of copolymers onto graphene by miniemulsion polymerization for conductive polymer composites: improved electrical conductivity and compatibility induced by interfacial distribution of graphene, Polymer Chem. 4 (10) (2013) 2939–2944.
[16] S.R. Athreya, K. Kalaitzidou, S. Das, Processing and characterization of a carbon black-filled electrically conductive Nylon-12 nanocomposite produced by selective laser sintering, Mater. Sci. Eng. A 527 (10) (2010) 2637–2642.
[17] M. Sumita, K. Sakata, S. Asai, K. Miyasaka, H. Nakagawa, Dispersion of fillers and the electrical conductivity of polymer blends filled with carbon black, Polym. Bull. 25 (2) (1991) 265–271.
[18] R. Haggenmueller, C. Guthy, J.R. Lukes, J.E. Fischer, K.I. Winey, Single wall carbon nanotube/polyethylene nanocomposites: Thermal and electrical conductivity, Macromolecules 40 (7) (2007) 2417–2421.
[19] E. Kymakis, G.A. Amaratunga, Electrical properties of single-wall carbon nanotube-polymer composite films, J. Appl. Phys. 99 (8) (2006) 084302.
[20] R.A. Khare, A.R. Bhattacharyya, A.R. Kulkarni, M. Saroop, A. Biswas, Influence of multiwall carbon nanotubes on morphology and electrical conductivity of PP/ABS blends, J. Polymer Sci. Part B 46 (21) (2008) 2286–2295.
[21] M. Wang, K. Zhang, X.-X. Dai, Y. Li, J. Guo, H. Liu, G.-H. Li, Y.-J. Tan, J.-B. Zeng, Z. Guo, Enhanced electrical conductivity and piezoresistive sensing in multi-wall carbon nanotubes/polydimethylsiloxane nanocomposites via the construction of a self-segregated structure, Nanoscale 9 (31) (2017) 11017–11026.
[22] M. Karttunen, P. Ruuskanen, V. Pitkänen, W.M. Albers, Electrically conductive metal polymer nanocomposites for electronics applications, J. Electron. Mater., 37, (7) 951–954.
[23] S.-Z. Guo, K. Qiu, F. Meng, S.H. Park, M.C. McAlpine, 3D printed stretchable tactile sensors, Adv. Mater. 29 (27) (2017) 1701218.
[24] H. Wei, X. Cauchy, I.O. Navas, Y. Abderrafai, K. Chizari, U. Sundararaj, Y. Liu, J. Leng, D. Therriault, Direct 3D printing of hybrid nanofiber-based nanocomposites for highly conductive and shape memory applications, ACS Appl. Mater. Interfaces 11 (27) (2019) 24523–24532.
[25] G. Sui, D. Liu, Y. Liu, W. Ji, Q. Zhang, Q. Fu, The dispersion of CNT in TPU matrix with different preparation methods: solution mixing vs. melt mixing, Polymer 182 (2019) 121838.
[26] P. Pötschke, F. Mothes, B. Krause, B. Voit, Melt-mixed PP/MWCNT composites: influence of CNT incorporation strategy and matrix viscosity on filler dispersion and electrical resistivity, Polymers 11 (2) (2019) 189.
[27] A. Funck, W. Kaminsky, Polypropylene carbon nanotube composites by in situ polymerization, Compos. Sci. Technol. 67 (5) (2007) 906–915.
[28] Z. Mousavi, M.-C. Heuzey, M.R. Kamal, E. Flahaut, P.J. Carreau, Rheological, electrical, and dynamic thermomechanical properties: Comparison between multiwall and double-wall carbon nanotubes in polylactide and polyamide 11, Phys. Fluids 33 (11) (2021) 113103.
[29] I. Krupa, J. Prokeš, I. Křivka, Z. špitalský, Electrically conductive polymeric composites and nanocomposites, in: Handbook of Multiphase Polymer Systems, 2011, pp. 425–477.
[30] H. Wei, X. Cauchy, I.O. Navas, Y. Abderrafai, K. Chizari, U. Sundararaj, Y. Liu, J. Leng, D. Therriault, Direct 3D printing of hybrid nanofiber-based nanocomposites for highly conductive and shape memory applications, ACS Appl. Mater. Interfaces 11 (27) (2019) 24523–24532.
[31] H. Pang, L. Xu, D.-X. Yan, Z.-M. Li, Conductive polymer composites with segregated structures, Prog. Polym. Sci. 39 (11) (2014) 1908–1933.
[32] M.J. Toghchi, C. Campagne, A. Cayla, P. Bruniaux, C. Loghin, I. Cristian, L. Burgnies, Y. Chen, Electrical conductivity enhancement of hybrid PA 6,6 composite containing multiwall carbon nanotube and carbon black for shielding effectiveness application in textiles, Synth. Met. 251 (2019) 75–84.
[33] B.P. Grady, Carbon Nanotube-Polymer Composites: Manufacture, Properties, and Applications, John Wiley & Sons, 2011.
[34] T. Villmow, P. Pötschke, S. Pegel, L. Häussler, B. Kretzschmar, Influence of twin-screw extrusion conditions on the dispersion of multi-walled carbon nanotubes in a poly(lactic acid) matrix, Polymer 49 (16) (2008) 3500–3509.
[35] B. Krause, P. Pötschke, L. Häuß ler, Influence of small scale melt mixing conditions on electrical resistivity of carbon nanotube-polyamide composites, Compos. Sci. Technol. 69 (10) (2009) 1505–1515.
[36] B. Krause, C. Barbier, K. Kunz, P. Pötschke, Comparative study of single-walled, multiwalled, and branched carbon nanotubes melt mixed in different thermoplastic matrices, Polymer 159 (2018) 75–85.
[37] S. Paszkiewicz, A. Szymczyk, D. Pawlikowska, J. Subocz, M. Zenker, R. Masztak, Electrically and thermally conductive low density polyethylene-based nanocomposites reinforced by MWCNT or hybrid MWCNT/graphene nanoplatelets with improved thermo-oxidative stability, Nanomaterials 8 (4) (2018) 264.
[38] J. Huang, C. Mao, Y. Zhu, W. Jiang, X. Yang, Control of carbon nanotubes at the interface of a co-continuous immiscible polymer blend to fabricate conductive composites with ultralow percolation thresholds, Carbon 73 (2014) 267–274.
[39] T.-W. Lee, Y.G. Jeong, Enhanced electrical conductivity, mechanical modulus, and thermal stability of immiscible polylactide/polypropylene blends by the selective localization of multi-walled carbon nanotubes, Compos. Sci. Technol. 103 (2014) 78–84.
[40] R. Cardinaud, T. McNally, Localization of MWCNTs in PET/LDPE blends, Eur. Polym. J. 49 (6) (2013) 1287–1297.
[41] Y.-M. Weng, M.-J. Chen, W. Chen, Antimicrobial food packaging materials from poly(ethylene-co-methacrylic acid), LWT-Food Sci. Technol. 32 (4) (1999) 191–195.
[42] E. Cohen, A. Ophir, S. Kenig, C. Barry, J. Mead, Pyridine-modified polymer as a non-covalent compatibilizer for multi-walled CNT/poly [ethylene-co-(methacrylic acid)] composites fabricated by direct melt mixing, Macromol. Mater. Eng. 298 (4) (2013) 419–428.
[43] N.A.M. Radzuan, A.B. Sulong, J. Sahari, A review of electrical conductivity models for conductive polymer composite, Int. J. Hydrogen Energy 42 (14) (2017) 9262–9273.
[44] P. Pötschke, T. Villmow, B. Krause, Melt mixed PCL/MWCNT composites prepared at different rotation speeds: Characterization of rheological, thermal, and electrical properties, molecular weight, MWCNT macrodispersion, and MWCNT length distribution, Polymer 54 (12) (2013) 3071–3078.
[45] K. Dydek, P. Latko-Durałek, A. Sulowska, M. Kubiś, S. Demski, P. Kozera, B. Sztorch, A. Boczkowska, Effect of processing temperature and the content of carbon nanotubes on the properties of nanocomposites based on polyphenylene sulfide, Polymers 13 (21) (2021) 3816.

[46] Y. Pan, L. Li, S.H. Chan, J. Zhao, Correlation between dispersion state and electrical conductivity of MWCNTs/PP composites prepared by melt blending, Composites A 41 (3) (2010) 419–426.
[47] S. Pegel, P. Pötschke, G. Petzold, I. Alig, S.M. Dudkin, D. Lellinger, Dispersion, agglomeration, and network formation of multiwalled carbon nanotubes in polycarbonate melts, Polymer 49 (4) (2008) 974–984.
[48] P.B. Tambe, A.R. Bhattacharyya, A.R. Kulkarni, The influence of melt-mixing process conditions on electrical conductivity of polypropylene/multiwall carbon nanotubes composites, J. Appl. Polym. Sci. 127 (2) (2013) 1017–1026.
[49] Z. Tang, S. Jia, C. Zhou, B. Li, 3D printing of highly sensitive and large-measurement-range flexible pressure sensors with a positive piezoresistive effect, ACS Appl. Mater. Interfaces 12 (25) (2020) 28669–28680.
[50] M. Abshirini, M. Charara, Y. Liu, M. Saha, M.C. Altan, 3D printing of highly stretchable strain sensors based on carbon nanotube nanocomposites, Adv. Eng. Mater. 20 (10) (2018) 1800425.
[51] M. Rafiee, R. Farahani, D. Therriault, Multi-material 3D and 4D printing: A survey, Adv. Sci. (2020) 1902307.
[52] Z. Wang, X. Guan, H. Huang, H. Wang, W. Lin, Z. Peng, Full 3D printing of stretchable piezoresistive sensor with hierarchical porosity and multimodulus architecture, Adv. Funct. Mater. 29 (11) (2019) 1807569.
[53] S. Mousavi, D. Howard, F. Zhang, J. Leng, C.H. Wang, Direct 3D printing of highly anisotropic, flexible, constriction-resistive sensors for multidirectional proprioception in soft robots, ACS Appl. Mater. Interfaces 12 (13) (2020) 15631–15643.
[54] K. Gnanasekaran, T. Heijmans, S. Van Bennekom, H. Woldhuis, S. Wijnia, G. De With, H. Friedrich, 3D printing of CNT-and graphene-based conductive polymer nanocomposites by fused deposition modeling, Appl. Mater. Today 9 (2017) 21–28.
[55] R. Calderon-Villajos, A. Lopez, L. Peponi, J. Manzano-Santamaria, A. Urena, 3D-printed self-healing composite polymer reinforced with carbon nanotubes, Mater. Lett. 249 (2019) 91–94.
[56] DuPont, Inc. 1007 Market Street, Wilmington, D.E. 19899, USA, Technical Data: DuPont Nucrel 2940 ethylene-methacrylic acid copolymer resin.
[57] 4 5060 Sambreville Belgium Nanocyl SA Rue de l'Essor, Technical data: NC7000™ multiwall carbon nanotubes, 2016.
[58] S. Kim, G. Mulholland, M. Zachariah, Density measurement of size selected multiwalled carbon nanotubes by mobility-mass characterization, Carbon 47 (5) (2009) 1297–1302.
[59] B. Earp, D. Dunn, J. Phillips, R. Agrawal, T. Ansell, P. Aceves, I. De Rosa, W. Xin, C. Luhrs, Enhancement of electrical conductivity of carbon nanotube sheets through copper addition using reduction expansion synthesis, Mater. Res. Bull. 131 (2020) 110969.
[60] J.-K. Kim, Y. Zhang, D.-W. Lee, A smart microfour-point probe with ultrasharp in-plane tips, Rev. Sci. Instrum. 80 (4) (2009) 045107.
[61] R. Socher, B. Krause, M.T. Müller, R. Boldt, P. Pötschke, The influence of matrix viscosity on MWCNT dispersion and electrical properties in different thermoplastic nanocomposites, Polymer 53 (2) (2012) 495–504.
[62] A. del Bosque, R. Calderon-Villajos, M. Sanchez, A. Urena, Multifunctional carbon nanotubes-reinforced surlyn nanocomposites: A study of strain-sensing and self-healing capabilities, Nanomaterials 12 (16) (2022).
[63] W. Zhang, A.A. Dehghani-Sanij, R.S. Blackburn, Carbon based conductive polymer composites, J. Mater. Sci. 42 (10) (2007) 3408–3418.
[64] M.H. Al-Saleh, U. Sundararaj, A review of vapor grown carbon nanofiber/polymer conductive composites, Carbon 47 (1) (2009) 2–22.
[65] J. Jyoti, S. Dhakate, B.P. Singh, Phase transition and anomalous rheological properties of graphene oxide-carbon nanotube acrylonitrile butadiene styrene hybrid composites, Composites B 154 (2018) 337–350.
[66] M. Bertolino, D. Battegazzore, R. Arrigo, A. Frache, Designing 3D printable polypropylene: material and process optimisation through rheology, Addit. Manuf. 40 (2021) 101944.
[67] U. Devi, R. Pejman, Z.J. Phillips, P. Zhang, S. Soghrati, K.B. Nakshatrala, A.R. Najafi, K.R. Schab, J.F. Patrick, A microvascular-based multifunctional and reconfigurable metamaterial, Adv. Mater. Technol. 6 (11) (2021) 2100433.
[68] S. Meure, D.-Y. Wu, S.A. Furman, FTIR study of bonding between a thermoplastic healing agent and a mendable epoxy resin, Vib. Spectrosc. 52 (1) (2010) 10–15.
[69] S. Meure, R.J. Varley, D.Y. Wu, S. Mayo, K. Nairn, S. Furman, Confirmation of the healing mechanism in a mendable EMAA–epoxy resin, Eur. Polym. J. 48 (3) (2012) 524–531.
[70] K. Pingkarawat, C. Dell'Olio, R. Varley, A. Mouritz, Poly(ethylene-co-methacrylic acid) (EMAA) as an efficient healing agent for high performance epoxy networks using diglycidyl ether of bisphenol A (DGEBA), Polymer 92 (2016) 153–163.
[71] M. Rafiee, F. Granier, R. Tao, A. Bhérer-Constant, G. Chenier, D. Therriault, Multi-material, multi-process, planar, and nonplanar additive manufacturing of piezoelectric devices, Adv. Eng. Mater. (2022) 2200294.
[72] M.H. Al-Saleh, U. Sundararaj, Electromagnetic interference shielding mechanisms of CNT/polymer composites, Carbon 47 (7) (2009) 1738–1746.
[73] Z. Zeng, H. Jin, L. Zhang, H. Zhang, Z. Chen, F. Gao, Z. Zhang, Low-voltage and high-performance electrothermal actuator based on multi-walled carbon nanotube/polymer composites, Carbon 84 (2015) 327–334.
[74] M. Safaei, H.A. Sodano, S.R. Anton, A review of energy harvesting using piezoelectric materials: state-of-the-art a decade later (2008–2018), Smart Mater. Struct. 28 (11) (2019) 113001.